PCCP

PAPER

View Article Online
View Journal | View Issue

Cite this: *Phys. Chem. Chem. Phys.*, 2026, **28**, 1173

Azothiophene-based molecular switches: influence of substituent position and solvent environment on photophysical behavior†

Xin Zhang, Konstantinos T. Kotoulas, P. M. Anuththara Bandaranayake, Dilani Chathumalee, Nuha Ehsan, Patrick R. Huddleston, John D. Wallis and Carole C. Perry *

Stimuli-responsive materials have attracted much attention in the design of 'smart' materials that can undergo reversible changes in their physical and/or chemical characteristics upon exposure to an external stimulus such as light. Notable examples include azobenzenes, spiropyrans, dithienylethenes and stilbenes. We have previously shown that azothiophene esters also undergo efficient $E \leftrightarrow Z$ photoisomerization under both ultraviolet and visible light sources. In this contribution a series of five novel molecular photoswitches, comprising two 3,3′-disubstituted azothiophenes and three hemi-azothiophenes was synthesized and characterized. The effect of substitution position and aromatic ring bulk on photoswitching behavior was explored. Photophysical performance is rationalized through X-ray crystallography, solvent-parameter modelling, and tautomerism studies, providing comprehensive insight into how molecular structure and environment govern the switching efficiency of azothiophene-based dyes. Increasing conjugation through bulkier aromatic substitution leads to a bathochromic shift in the absorption maximum (λ_{max}), enabling visible-light-activated isomerization. We show that these azothiophenes have varying photoswitch ability, with diacid derivatives exhibiting superior solvatochromic behavior including an example of a clear pH-dependent color change, suggesting potential application for these molecules as pH sensors or indicators. The data presented suggests a strategy for the rational design of tunable azothiophene photoswitches, with potential application in photoresponsive materials and optical sensing.

Received 7th August 2025,
Accepted 24th November 2025

DOI: 10.1039/d5cp03027g

rsc.li/pccp

1. Introduction

In recent years, stimuli-responsive materials have attracted much attention in the design of 'smart' materials that are capable of undergoing reversible changes in their physical and/or chemical characteristics upon exposure to external stimuli.[1–5] These stimuli may be physical, chemical, biological, or environmental, including changes in pH, light, temperature, and magnetic or electric fields.[6] Among these, light is of particular interest due to its non-invasive nature, precise spatial and temporal control, and rapid response times.[7–9] Several groups have reported photoresponsive systems that undergo conformational changes or electronic rearrangements—such as *trans* (*E*)–*cis* (*Z*) isomerization or bond cleavage when molecules are exposed to specific wavelengths of light.[10] Notable examples include azobenzenes, spiropyrans, azoheteroarenes, dithienylethenes and stilbenes.[11–14] For instance, azobenzene derivatives are known for their rapid and reversible isomerization between the *trans*- and *cis*-forms under UV (approx. 365 nm) or visible irradiation (450 nm).[8,15,16] The substitution position and substituent on azobenzene allow precise control over different switching properties, including absorption, emission, photostationary state (PSS), quantum yield, and thermal stability.[16] In principle, the photoisomerization properties can be modulated by tuning the energy levels of the n and π* orbitals of the *E* and *Z* isomers. *Ortho*- and *para*-positioned electron-withdrawing groups decrease repulsive interactions between the nitrogen lone pairs in the *Z* isomer.[17] Azobenzenes have been used in a wide range of emerging applications, such as biomedical, photo-controlled drug delivery, tissue engineering, and biodegradable systems based on enzymatic cleavage of the azo bond.[18–24] For successful implementation of photoswitches in a biological environment, they must meet critical requirements: selective photoisomerization capability, biocompatible

Department of Chemistry and Forensic Science, Nottingham Trent University, Nottingham, UK. E-mail: carole.perry@ntu.ac.uk

† This article is dedicated to Dr Patrick R. Huddleston, who worked on azothiophenes and other aspects of organic chemistry at Nottingham Trent University for over 58 years, and who passed away unexpectedly during this project. He was actively involved in this study and in his own research at the time of his death. His many contributions to research over the years are greatly appreciated by his colleagues.

irradiation characteristics, thermal stability, and robust fatigue resistance.[25,26]

Beyond traditional azobenzene derivatives, researchers have explored other heterocyclic dyes as alternatives. These include a variety of combinations of five-membered rings – furan, thiophene, pyrrole, thioazole, and imidazole – investigated as diazo components for their nonlinear optical properties and potential applications in optical data storage.[27–30] Among these, thiophene-based systems have gained significant interest due to their ability to confer mesomorphic properties,[31] synthetic versatility, and environmental stability.[32] Thiophene-derived photoswitches exhibit enhanced fatigue resistance and superior photoisomerization efficiency, attributed to the well-separated *E* and *Z* isomer absorption bands.[33]

However, as opposed to well-studied azobenzenes, the photophysical properties of thiophene-containing heteroazoarenes remain relatively underexplored, particularly regarding the systematic tailoring photoswitch performance through substituent effects and their influence on photophysical and photochemical properties.[34–37] A comprehensive understanding of the substitution effects in thiophene-based compound is crucial for their rational design and integration into functional material systems.[28] Examples of recent studies include exploring the effects of electron-donating and withdrawing substituents on the thermal *Z–E* isomerization kinetics of thiophenylazobenzenes, with $\pi \rightarrow \pi^*$ absorption being extended up to 414 nm,[38] and exploration of the photophysical properties of the thiophene-based photoswitch TA–OH across solvents of varying polarity.[39] A recent study by Wegner *et al.* further expands on this by systematically investigating how alkoxy substitution modulates melting points and photoisomerization efficiency in azothiophenes, providing valuable insights into their structure–property relationships and potential for molecular solar thermal phase-change materials (MOST–PCM) applications.[40]

Our research group has previously reported a photoswitchable dye based on the azothiophene scaffold.[41] Both experimental and computational studies showed that photoisomerization between *trans* and *cis* isomers can be achieved upon irradiation using either ultraviolet or visible light sources.

Following upon, this study systematically investigates the influence of substitution position and aromatic ring bulk on the photophysical properties of five novel azothiophenes (four diacids, one monoacid), uncovering the key design principles for tailored molecular photoswitches. We demonstrate that extending conjugation *via* bulky aromatic substitutions induces a pronounced bathochromic shift in the absorption maximum (λ_{max}), enabling visible-light-activated isomerization. Furthermore, the photo-induced half-life of the metastable *Z* isomer can be modulated by solvent polarity, offering tunable switching dynamics. We show that these azothiophenes have varying photoswitch ability, with diacid derivatives exhibiting superior solvatochromic behavior including an example of a clear pH-dependent color change, highlighting their potential as pH sensors or indicators. These very favorable properties render azothiophenes as particularly promising new photoswitch scaffolds for advanced applications, including those incorporation into biomolecule systems. We provide a mechanistic framework linking molecular structure and microenvironment to photophysical performance by combining X-ray crystallography, solvent-parameter modelling, and tautomerism studies. Our findings establish the understanding of structural and environmental interplays that govern the switching efficiency of azothiophenes, casting new light on molecular design principles for photoresponsive materials.

2. Experimental

2.1 Materials

Chemicals used for synthesis and analysis were purchased from Sigma-Aldrich. All materials were of analytical grade and directly used without further purification.

2.2 Synthesized azothiophene molecules

Following on from photophysical studies on azothiophene by Huddleston *et al.*,[41] five new azothiophenes (four diacids, one monoacid) were synthesized and their behavior compared to the published diester. The molecular structure and color of the synthesized molecules labeled **1a–5a** together with that of the parent, labeled as **1b**, is presented in Fig. 1.

2.2.1 General. Solution NMR spectra were measured on a Jeol ECLIPSE ECX or ECZ 400 spectrometer at 400 MHz for ^{1}H and at 100.6 MHz for ^{13}C using $CDCl_3$, THF-d_8 or DMSO-d_6 as the solvent and tetramethylsilane (TMS) as standard unless otherwise stated and measured in p.p.m. downfield from TMS with coupling constants reported in Hz. IR spectra were recorded on a PerkinElmer spectrum 100 FT-IR spectrometer using attenuated total reflection sampling and are reported in cm^{-1} (both NMR and IR spectra are provided in the SI). High resolution mass spectra were recorded at the National Mass Spectrometry Facility at the University of Swansea. Melting points measurements were carried out on a Stuart SMP10 apparatus, data were recorded to the nearest 0.5 °C. Crystal structures of **1a** and two polymorphs of **1b** were determined from data collected on single crystals using CuKα radiation on a Rigaku XtaLAB Synergy-DW VHF system equipped with a HyPix-Arc 100 detector at low temperature. Full details, including crystal data, are provided in the SI.

2.2.2 (*E*)-3,3′-Azothiophene-2,2′-dicarboxylic acid (1a)

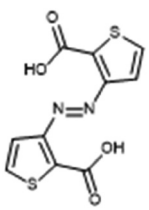

(*E*)-2,2′-Bis(methoxycarbonyl)-3,3′-azothiophene (**1b**)[42] (0.99 g, 3.19 mmol), 4 M aqueous sodium hydroxide (4.6 mL) and ethanol (3.4 mL) were heated and stirred together at 90 °C for 30 min. The red color of the ester changed to yellow during this time. The reaction was cooled and diluted with water to 40 mL

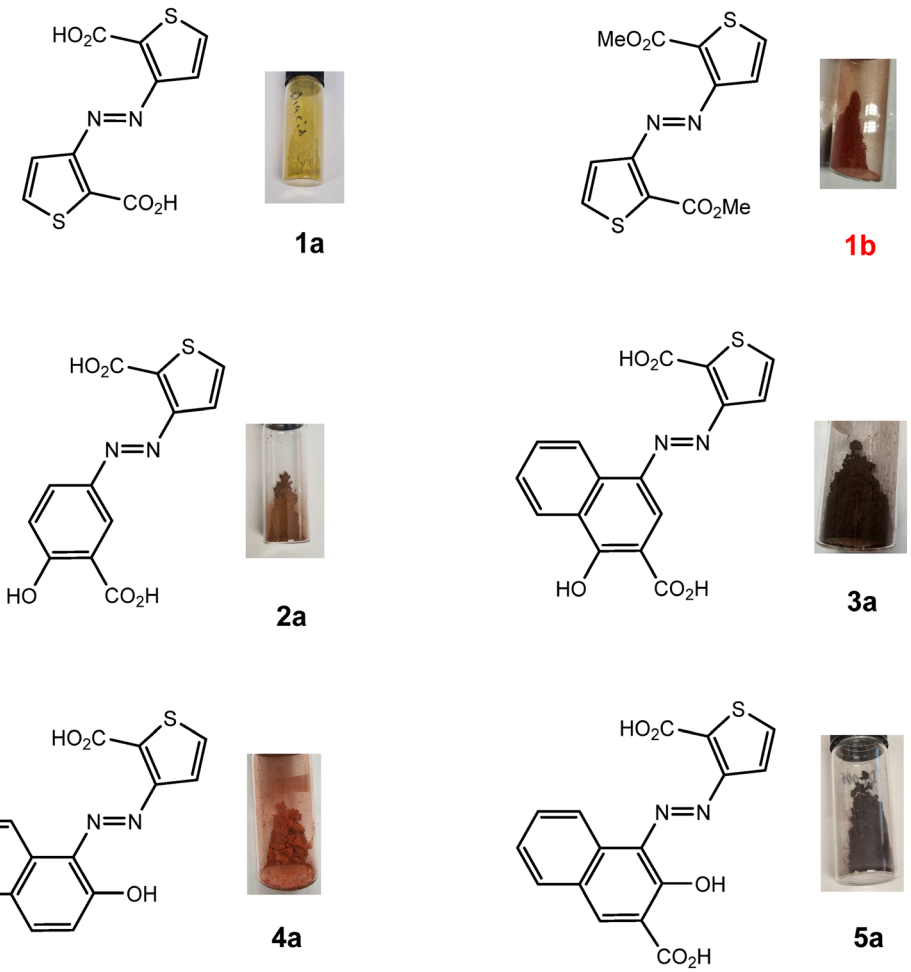

Fig. 1 Molecular structure and color of the five new azothiophenes (**1a**–**5a**), along with the parent published azothiophene diester (**1b**).

and acidified with 4 M hydrochloric acid. The resultant precipitate was filtered and dried under vacuum, giving **1a** as a yellow-green solid (0.87 g, 97%), m.p. 156–158 °C; δ_H (400 MHz, THF-d_8): 7.69 (2H, d, J = 5.6, 5-,5′-*H*), 7.52 (2H, d, J = 5.5, 4-,4′-*H*); δ_C (100.6 MHz, THF-d_8): 161.7 (2 x *C*═O), 156.4 (3-,3′-*C*), 134.2 (2-,2′-*C*), 131.1 (5-,5′-*C*), 119.6 (4-,4′-*C*); ν_{max}: 3109, 3094, 2965 v. br, 1719, 1675, 1524, 1495, 1458, 1430, 1393, 1304, 1290, 1230, 1210, 1080, 1063, 1027, 877, 776, 756, 729, 693, 663, 605, 553, 495, 465; HRMS: (−ve ion nanospray): found: 584.9291 (50%), calcd for $[2M - 2H + Na]^-$: 584.9285; 258.9617 (38%), calcd for $[M - CO_2H - H + Na]^-$: 258.9617; 192.9900 (100%), calcd for $[M - 2CO_2 - H]^-$: 192.9900.

2.2.3 (*Z*)-3,3′-Azothiophene-2,2′-dicarboxylic acid (*Z*-1a). On irradiation of an NMR sample of the *E*-isomer of **1a** in THF-d_8 at 365 nm for 20 min. using a Convoy S2+ Nichia ultraviolet LED flashlight, *ca.* 62% of the sample converted to the *Z*-isomer. Thermal half-life in the dark was estimated as 35 days by successive NMR measurements. *Z*-**1a**: δ_H (400 MHz, THF-d_8): 10.93 (2H, br, 2 x CO_2*H*), 7.44 (2H, d, J = 5.2, 5-,5′-*H*), 6.42 (2H, d, J = 5.2, 4-,4′-*H*); δ_C (100.6 MHz, THF-d_8): 162.1 (2 x *C*═O), 158.9 (3-,3′-*C*), 134.3 (2-,2′-*C*), 131.4 (5-,5′-*C*), 120.4 (4-,4′-*C*).

2.2.4 Dimethyl (*E*)-3,3′-Azothiophene-2,2′-dicarboxylate (1b). Prepared as described.[42] δ_H (400 MHz, $CDCl_3$): 7.53 (2H, d, J = 5.3, 4-,4′-*H*), 7.46 (2H, d, J = 5.3, 5-,5′-*H*), 3.96 (6H, s, 2 x O–CH_3); δ_C (100.6 MHz, $CDCl_3$): 161.6 (2 x *C*═O), 156.8 (d, $^2J_{C,H}$ = 9.6, 3-,3′-*C*), 131.4 (2-,2′-*C*), 129.9 (dd, $^1J_{C,H}$ = 187.9, $^2J_{C,H}$ = 6.0, 5-,5′-*C*), 118.8 (dd, $^1J_{C,H}$ = 176.0, $^2J_{C,H}$ = 3.8, 4-,4′-*C*), 52.5 (q, $^1J_{C,H}$ = 147.2, 2 x O*C*H_3).

2.2.5 Preparation of 2-(methoxycarbonyl)-thiophene-3-diazonium chloride (26.6 mmol scale) for use in preparation of (2a)–(5a). Methyl 2-aminothiophene-3-carboxylate (4.18 g, 26.6 mmol) was dissolved in concentrated hydrochloric acid (6.9 mL, *ca.* 82 mmol) and diluted with water (6.4 mL). The stirred solution was cooled to 0 °C and treated with sodium nitrite (1.92 g, 26.6 mmol) and stirred for 15 min at 0 °C.

2.2.6 3-((3′-Carboxy-4-hydroxyphenyl)diazenyl)thiophene-2-carboxylic acid (2a)

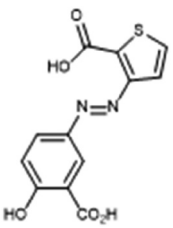

. An ice-cold solution of salicylic acid (3.66 g, 20 mmol) and

sodium hydroxide (3.20 g, 80 mmol) in water (40 mL) was added to an aqueous solution of freshly prepared 2-(methoxycarbonyl)-thiophene-3-diazonium (26.6 mmol) at 0 °C. The solution was stirred and allowed to come to room temperature over 2 h. The pH was adjusted to 5–6 by addition of 2 M hydrochloric acid and the precipitate formed was filtered and dried to give crude methyl (*E*)-3-((3′-carboxy-4′-hydroxyphenyl)-diazenyl)thiophene-2-carboxylate (4.70 g, 58%). This ester (4.50 g, 14.7 mmol) was heated and stirred with 4 M sodium hydroxide (20 mL) and ethanol (15 mL) at 90 °C for 30 min. After cooling and acidification with 4 M hydrochloric acid, the resultant precipitate was collected, dissolved in methanol, precipitated with water and dried to give **2a** (3.78 g, 84%) as a yellow brown powder, m.p. 78–80 °C; δ_H (400 MHz, DMSO-d_6): 8.33 (1H, d, J = 2.4, 2′-*H*), 8.03 (1H, dd, J = 8.8, 2.4, 6′-*H*), 7.85 (1H, d, J = 5.6, 5-*H*), 7.39 (1H, d, J = 5.6, 4-*H*), 7.16 (1H, d, J = 8.8, 5′-*H*); δ_C (100.6 MHz, DMSO-d_6): 171.4 (3′-*C*O_2H), 164.1 (4′-*C*), 162.3 (2-*C*O_2H), 155.4 (3-*C*), 144.9 (1′-*C*), 131.4 (5-*C*), 131.3 (2-*C*), 129.0 (6′-*C*), 126.6 (2′-*C*), 118.7 (4-*C*), 118.6 (5′-*C*), 113.9 (3′-*C*); (thus, in DMSO-d_6, **2a** is present mainly as the *azo* tautomer.); ν_{max}: 2923 br (3300–2500), 1713, 1673, 1585, 1561, 1487, 1425, 1364, 1341, 1260, 1218, 1184, 1095, 1072, 1010, 833, 775, 722, 670, 648, 581, 551, 514; HRMS: (−ve ion nanospray): found: 312.9988 (10%), calcd for $[M - 2H + Na]^-$: 312.9901; 291.0081 (100%). Calcd for $[M - H]^-$: 291.0081; 247.0184 (43%), calcd for $[M - CO_2H]^-$: 247.0183.

2.2.7 1-Hydroxy-4-((2-(methoxycarbonyl)thiophen-3-yl)diazenyl)-2-naphthoic acid (3a)

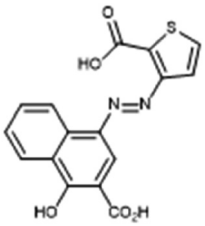

Following the method for **1a** but using 1-hydroxy-2-naphthoic acid (3.76 g, 20 mmol) instead of salicylic acid gave methyl (*E*)-3-((3′-carboxy-4′-hydroxynaphthalen-1-yl)diazenyl)thiophene-2-carboxylate (5.40 g, 76%). This ester (5.00 g, 14 mmol) was hydrolysed using the method above to give **3a** (4.05 g, 84%) as a purple powder, m.p. 185–187 °C; δ_H (400 MHz, DMSO-d_6): 18.34 (1H, br s, N-*H*), 8.86 (1H, d, J = 8.4, 8′-*H*), 8.47 (1H, s, 2′-*H*), 8.34 (1H, d, J = 8.0, 5′-*H*), 7.88 (1H, d, J = 5.0, 5-*H*), 7.66 (1H, t, J = 7.6, 7′-*H*), 7.62 (1H, d, J = 5.0, 4-*H*), 7.49 (1H, t, J = 7.2 Hz, 6′-*H*); δ_C (100.6 MHz, DMSO-d_6): 174.7 (4′-*C*), 170.6 (3′-*C*O_2H), 162.5 (2-*C*O_2H), 157.2 (3-*C*), 134.7 (8a′-*C*), 134.1 (4a′-*C*), 131.6 (5-*C*), 129.7 (7′-*C*), 127.9 (1′-*C*), 126.7 (2-*C*), 124.7 (5′-*C*), 124.6 (6′-*C*), 122.7 (8′-*C*), 119.5 (4-*C*), 119.3 (2′-*C*), 109.9 (3′-*C*) (Thus, in DMSO-d_6, **3a** is present mainly as the hydrazo tautomer.); ν_{max}: 3449 br, 3079, 2960, 2925, 2856, 1725, 1704, 1623, 1577, 1507, 1434, 1394, 1276, 1252, 1189, 1120, 1099, 1068, 1030, 998, 874, 781, 759, 736, 660, 599, 546, 488; HRMS (−ve ion nanospray): found: 341.0240 (100%), calcd for $[M - H]^-$: 341.0238.

2.2.8 2-Hydroxy-3-((2-(methoxycarbonyl)thiophen-3-yl)diazenyl)-1-naphthoic acid (4a)

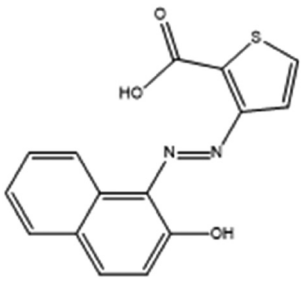

Following the method for **1a** but using 2-hydroxy-1-naphthoic acid (1.88 g, 10 mmol) instead of salicylic acid, and working on a 50% scale, gave methyl (*E*)-3-(2′-hydroxynaphth-1′-yl)diazenyl)thiophene-2-carboxylate (2.53 g, 81%). This ester (2.00 g, 6.4 mmol) was hydrolysed using the method above to give **4a** as an orange-red solid, m.p. 220–222 °C; δ_H (400 MHz, DMSO-d_6): 16.15 (1H, br s, N-*H*), 8.36 (1H, d, J = 8.0, 8′-*H*), 7.96 (1H, d, J = 5.6, 5-*H*), 7.86 (1H, d, J = 9.8, 4′-*H*), 7.84 (1H, d, J = 5.6, 4-*H*), 7.66 (1H, d, J = 7.6, 5′-*H*), 7.54 (1H, t, J = 7.6, 7′-*H*), 7.43 (1H, t, J = 7.4, 6′-*H*), 6.67 (1H, d, J = 9.8, 3′-*H*); δ_C (100.6 MHz, DMSO-d_6): 178.3 (2′-*C*), 163.2 (2-*C*O_2H), 147.9 (3-*C*), 142.6 (4′-C), 133.3 (5-C), 132.8 (8a′-C), 130.2 (1′-C), 129.6 (7′-C), 129.2 (5′-C), 128.3 (4a′-*C*), 127.1 (6′-*C*), 126.4 (3′-*C*), 122.1 (8′-*C*), 119.3 (4-*C*), 113.6 (2-*C*) (thus, in DMSO-d_6, **4a** is present mainly as the hydrazo tautomer); ν_{max}: 2981 v. br (3600–2300), 1686, 1531, 1488, 1446, 1409, 1334, 1317, 1253, 1198, 1152, 1142, 1090, 1074, 999, 918 br, 872, 856, 840 br, 772, 752, 726, 661, 640, 624, 541, 518, 487, 473, 454; HRMS (−ve ion nanospray): found: 297.0340 (100%), calcd for $[M - H]^-$: 297.0339; 253.0442 (85%), calcd for $[M - H - CO_2]^-$: 253.0441.

2.2.9 3-Hydroxy-4-((2-(methoxycarbonyl)thiophen-3-yl)diazenyl)-2-naphthoic acid (5a)

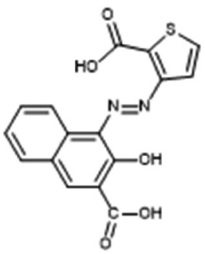

Following the method for **1a** but using 3-hydroxy-2-naphthoic acid (3.76 g, 20 mmol) instead of salicylic acid gave methyl (*E*)-3-(3′-carboxy-2′-hydroxynaphth-1′-yl)diazenyl)thiophene-2-carboxylate (4.61 g, 65%). This ester (4.50 g, 12.6 mmol) was hydrolysed using the method above to give **5a** (3.33 g, 77%) as a deep purple powder, m.p. 230–232 °C; δ_H (400 MHz, DMSO-d_6): 16.26 (1H, br s, N-*H*), 8.61 (1H, s, 4′-*H*), 8.43 (1H, d, J = 8.0, 8′-*H*), 8.01 (1H, d, J = 5.6, 5-*H*), 7.92 (1H, d, J = 7.6, 5′-*H*), 7.92 (1H, d, J = 5.6, 4-*H*), 7.69 (1H, t, J = 7.6, 7′-*H*), 7.52 (1H, t, J = 7.4, 6′-*H*); δ_C (100.6 MHz, DMSO-d_6): 176.1 (2′-*C*), 165.1 (3′-*C*O_2H), 163.1 (2′-*C*O_2H), 147.1 (4′-*C*), 146.9 (3-*C*), 134.3 (8a′-*C*), 133.6 (5-*C*), 131.9 (7′-*C*), 131.2 (5′-*C*), 130.0 (1′-*C*), 127.4 (6′-*C*), 126.4 (4a′-*C*), 126.1 (3′-*C*), 122.1 (8′-*C*), 119.5 (4-*C*), 115.1 (2-*C*) (Thus, in

DMSO-d_6, **5a** is present mainly as the hydrazo tautomer.); ν_{max}: 3103 br (3700–2300), 1715, 1685, 1609, 1596, 1552, 1497, 1450, 1443, 1421, 1387, 1326, 1264, 1199, 1171, 1116, 1041, 1021, 776, 756, 744, 720, 665, 654, 639, 513; HRMS (−ve ion nanospray): found 341.0239, calcd for $[M - H]^-$ 341.0238.

2.2.10 UV-vis spectroscopy and photoisomerization studies. All solutions were freshly prepared by dissolving the azothiophene derivatives in the chosen solvents, followed by sonication, prior to every UV-vis measurement, at the dedicated concentrations (4×10^{-5} M, if not otherwise stated). For the photoisomerization experiment, the solvents include DCM, NaOH aq. solution (1×10^{-4} M), while DMSO, acetonitrile, methanol, acetone, isopropanol, THF at concentrations of 4×10^{-5} M were employed for thermal stability study. The UV-vis absorption spectra were recorded on a VARIAN CARY 50-scan UV-Vis spectrophotometer from 200–1000 nm. The sample solutions were measured in QS High Precision Cells made of Quartz Suprasil, with an optical path length of 10 mm, from Hellma Analytics.

Photo-induced $E \leftrightarrow Z$ isomerization experiments were carried out using a Convoy S2+ Nichia flashlight with radiation at 365 nm (UV light source), and a warm tungsten lamp with broadband radiation centered at 530 nm (TL light source, 425–575 nm), respectively. Samples were exposed to TL light as the *E*–*Z* irradiation source, followed by placing in the dark to induce the *Z*–*E* conversion. Photoisomerization was achieved by irradiating samples with the appropriate light source with a home-built optical setup.

Due to instrumentational constraints, quantum yield measurements were not performed. Instead, the half-life of azothiophene **1a** was evaluated under two conditions: (1) thermal conversion in the dark at 20 °C ($t_{1/2}$, thermal) and (2) photo-induced conversion using a tungsten lamp (425–575 nm) ($t_{1/2}$, photo). UV-vis kinetic analysis was used for photo-induced measurements. Thermal half-lives for molecules **1a** and **1b** in THF-d_8 were determined *via* NMR spectroscopy, the spectra are provided in the SI.

2.2.11 pH-Driven tautomerism studies. Tautomerism as a function of pH was investigated by dissolving the chosen molecules in the solvent (DMSO, 1×10^{-2} M NaOH aq. solution) at 4×10^{-5} M. The acidic and basic conditions of aqueous dye solutions were achieved by adding varying amounts of HCl (10^{-1} M) and NaOH aq. solution (1, 10^{-1}, 10^{-2}, 10^{-3} M). The pH measurements of the aqueous dye solutions were recorded with a HI-2002 EDGE PH METER (Hanna Instruments Ltd). Their corresponding UV-vis spectra were taken using the same instrument as mentioned earlier.

2.2.12 Computational studies. All calculations were conducted using the Gaussian 16 program on the high-performance computer server Avicenna at Nottingham Trent University. Quantum density functional theory (DFT) calculations were performed with the RB3LYP/6-311++G(d,p) basis set and functional, as implemented in Gaussian 16. For each molecular system, the ground-state structure was determined through standard geometry minimization and vibrational frequency calculations were used to confirm that all bond vibrations were real. Default geometry convergence criteria on the Gaussian 16 program were, maximum force = 1.8×10^{-5} Hartree $Bohr^{-1}$, RMS force = 5×10^{-6} Hartree $Bohr^{-1}$, Maximum displacement = 6.85×10^{-4} Bohr, RMS displacement = 1.49×10^{-4} Bohr, predicted energy change = -9.041263×10^{-9}.

Time-dependent density functional theory (TD-DFT) was used within Gaussian 16 to extract the intensities of electronic transitions in the UV-vis spectral range. All the solvent phase calculations were performed on the optimized structure in the gas phase and solvent effects were considered implicitly using a polarizable continuum model (PCM). The computationally obtained minimum-energy structure was validated by comparing the calculated λ_{max} with experimental data, confirming the accuracy of the optimized geometry. The GaussView software package was used to visualize the calculated UV-vis spectra. The thermal isomerization energies were estimated using two computational approaches. The first method involved calculating the energy difference based on total electronic energies obtained from geometry optimizations of the *E* and *Z* isomers (Hartree Fock). The second approach employed thermochemical parameters derived from Gaussian calculations to estimate the free energy change associated with the $Z \rightarrow E$ isomerization reaction (Thermochemistry approach).

3. Results and discussion

From the ^{13}C NMR spectra in DMSO-d_6 compound **2a** is assigned as mainly in the azo form and compounds **3a–5a** to be mainly in the hydrazo form. This is most notably for the *C*–OH group (azo) or *C*═O group (hydrazo) (**2a**: 164.1; **3a–5a**: 174.7–178.3 ppm), and for the point of attachment of the azo group to the hydroxyaryl ring (*C*–N═N in the azo case, and *C*═N–NH in the hydrazo case) (**2a**: 146.9; **3a–5a**: 127.9–130.2 ppm). The assignments of **2a** as predominantly the azo tautomer, and of **3a–5a** as predominantly the hydrazo tautomers in DMSO-d_6 are chemically reasonable, since the hydrazo form for **2a** would involve disruption of the aromatic structure of its benzene ring, while for **3a–5a** the hydrazo form involves disruption of just one ring of the naphthalene group. In all four cases only one set of signals is observed. Compounds **4a** and **5a** show a peak at *ca.* 16 ppm which is probably due to N–H group which can form two intramolecular hydrogen bonds. Compound **3a** shows a similar peak at 18.34 ppm, again probably due to the N–H group, though there is only one intramolecular hydrogen bond in this case. There may well be a fast equilibrium between tautomers in compounds **2a–5a** with a small amount of the other form present, as has been extensively discussed by Lyčka.[43–46] For **4a** and **5a** interconversion between azo and hydrazo forms only requires the intramolecular transfer of a proton from O to N which has been studied in detail by Gilli *et al.*[47,48]

3.1 Photoswitching behavior

The photoswitching behavior of the azothiophene derivatives are given in Table 1. Particular attention was given to

Table 1 The spectroscopy and photoisomerization behaviours of all synthesized azothiophene derivatives in either DCM or NaOH aq. solution as the solvent at room temperature. Calculation of molar adsorption coefficient follows: $\varepsilon = A/cl$, $c = 4 \times 10^{-5}$ M, optical path $l = 1.0$ cm. *E*–*Z* illumination source

	Initial		Upon illumination (*E*–*Z*)				Upon illumination (*Z*–*E*)			
	λ π–π* (nm)	ε (10^{-3} cm^{-1} M^{-1})	λ π–π* (nm)	ε (10^{-3} cm^{-1} M^{-1})	λ n–π* (nm)	*E*–*Z* $\Delta\varepsilon$ (%)	λ π–π* (nm)	ε (10^{-3} cm^{-1} M^{-1})	λ n–π* (nm)	*Z*–*E* conversion (%)
1a[a,1]	377	1.31	377	0.52	—	**60.5**	377	0.76	—	≈57.9
1a[a,2]	352	2.45	352	0.88	434	**64.3**	352	2.05	—	≈83.8
1b[a,1]	345	5.56	345	3.44	460	**38.1**	345	5.53	—	≈99.6
2a[b,2]	440	1.72	440	1.68	—	2.5	440	1.73	—	≈100.5
3a[b,2]	508	2.30	508	1.96	—	14.8	508	2.02	—	≈87.6
4a[a,2]	481	0.76	481	0.59	—	22.4	481	0.73	—	≈95.7
5a[b,2]	498	1.15	498	1.15	—	0.5	498	1.16	—	≈100.3

[a] UV light. [b] Tungsten lamp. Solvent used 1: DCM, 2: NaOH aq. solution.

compounds containing carboxylic acid groups (**1a**, **2a**, **3a**, **4a**, **5a**), which were studied in alkaline NaOH aq. solution to disrupt any potential intramolecular hydrogen bond (IHB) that can otherwise impede isomerization.[49] Molecule **1a** shows a clear absorption at 377 nm (π–π*) prior to irradiation (Fig. 2a), while molecule **1b** exhibits a dominant absorption at 345 nm (π–π*) and a weaker band at 460 nm (n–π*) (Fig. 2b), indicating a thermal equilibrium mixture dominated by the *E* isomer.

Upon UV exposure, molecule **1a** showed clear $E \rightarrow Z$ isomerization, characterized by a decrease in π–π* intensity at 377 nm, whereas molecule **1b** showed a decrease in π–π* intensity accompanied by a concomitant increase in n–π* absorbance. Particularly, for the previously published azothiophene diester **1b**, re-irradiation with tungsten light resulted in recovery of the initial spectrum, indicating efficient reversible switching. However, molecule **1a**, tested in DCM, deviated from this observation. It exhibited limited reversibility and a large molar absorptivity change ($\Delta\varepsilon$ = 60.5%), yet could not fully regenerate the original spectrum upon $Z \rightarrow E$ irradiation.

To better understand this behavior, X-ray crystallographic analysis of **1a** and **1b** was undertaken. The crystal structure of diacid **1a** is monoclinic and in space group $P2_1/n$. It revealed the presence of a 1,6-intramolecular hydrogen bond between the azo nitrogen and an adjacent carboxylic acid proton, with geometry: O(2)–H(21): 0.87(7) Å, H(21)···N(1): 1.89(7) Å with angle at the H atom of 152(6)° and the O–H bond directed *trans* to the carbonyl bond, C(5)═O(1), of the acid group (Fig. 3a).

In contrast, the second carboxylic acid links molecules into chains along the *b* axis (Fig. 3b), by forming a hydrogen bond with the carbonyl oxygen O(1) of another molecule, with geometry: O(4)–H(41): 0.87(8) Å, H(41)···O(1, x, $y-1$, z): 1.84(8) Å with the angle at the H atom of 166(6)° and the O–H bond directed *cis* to the carbonyl bond, C(10)═O(3), as is more usually observed. This presence of an intramolecular hydrogen bond in the *E* isomer of **1a**, suggests that in its *Z* form, it is feasible that there could be one or two such intramolecular hydrogen bonds from the azo group to carboxylic acid groups which would stabilize the structure depending on the hydrogen bonding forming ability of the solvent.

It is rare to have a crystal structure with two conformations of a carboxylic acid. Of note is the smaller O–C═O angle (120.0(4°) when the O–H bond is *trans* to the C═O, compared to the more usual *cis* conformation (124.2(4°). The latter is in line with low temperature (<150 K) crystal structures of *ortho*-unsubstituted benzoic acid derivatives (123.5(8)°) in the Cambridge Structural Database.[50] Within this crystal structure there

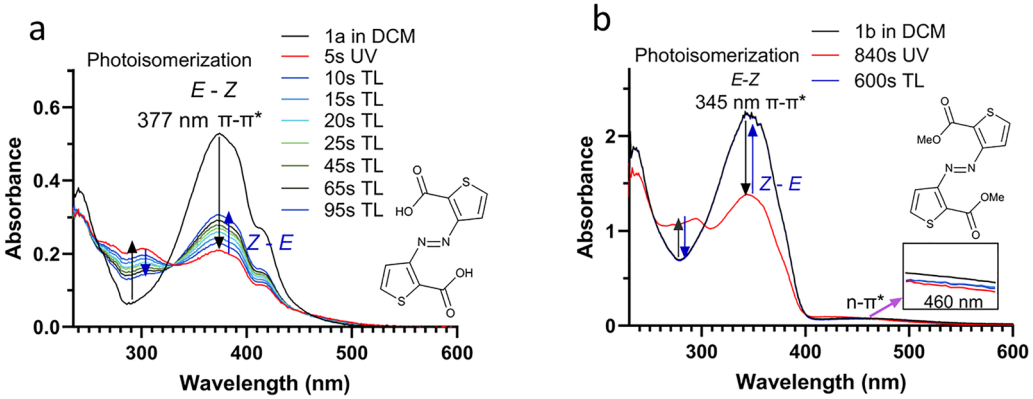

Fig. 2 Photoswitching behavior of azothiophenes (a) **1a** and (b) **1b** in DCM at room temperature. *Trans*–*cis* photoisomerization induced by UV irradiation, *cis*–*trans* induced by a tungsten lamp (TL).

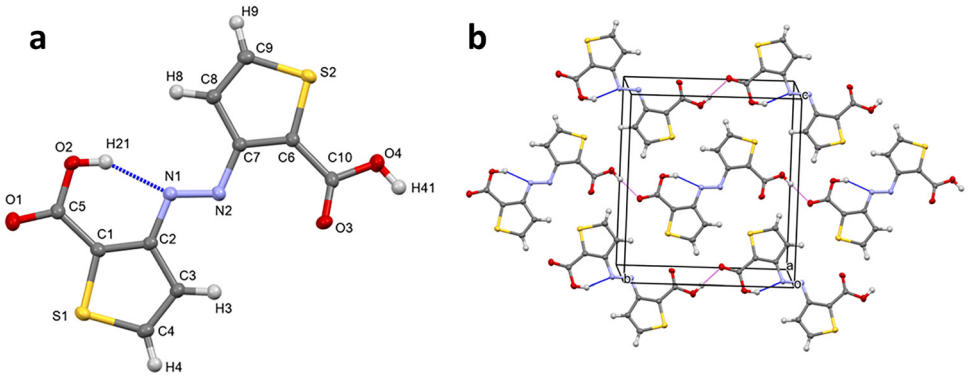

Fig. 3 X-ray crystallographic analysis of azothiophene **1a**, (a) molecular structure of diacid **1a** with anisotropic displacement parameters drawn at the 50% level; (b) view down the a axis showing the linking of molecules along the b axis by intermolecular hydrogen bonds (shown in violet), with intramolecular hydrogen bonds (shown in blue).

is one intramolecular (1,5) contact between a carbonyl oxygen and an azo nitrogen (2.886 Å), and two (1,5) contacts between a thiophene hydrogen and an azo nitrogen (2.60 and 2.69 Å). Similar to diester **1b**, the carboxylic acid group is bent away from the azo group (by 4.4 and 3.7°), and the azo group is bent towards the carboxylic acid (by 4.0 and 4.4°). Further crystallographic data is found in Tables S1–S5 and Fig. S1.

A comparison to the structure of the parent diester **1b** was possible though the diester **1b** crystallizes from THF as two polymorphs: a major monoclinic form (orange plates) and a minor triclinic form (colorless plates). These polymorphs exhibit slightly different molecular conformations and quite different crystal packing arrangements. In the orange polymorph, the molecule of **1b** is close to planar, sitting on a center of symmetry. Conversely, in the colorless polymorph, the entire molecule is crystallographically unique, with one thiophene ring tilted by 19.6° to the best plane of the thiophene-azo skeleton. In both polymorphs a carbonyl oxygen atom is directed towards an azo nitrogen atom. Full details and illustrations are given in the SI (Fig S2–S7 and Table S5).

To confirm the likely presence of intramolecular hydrogen bond in solution, compound **1a** was investigated in alkaline NaOH aq. solution where it was hypothesized that deprotonation of the carboxylic acid would disrupt the IHB between the –COOH group and the adjacent azo nitrogen. As shown in Fig. 4, the UV-vis spectrum revealed two well-resolved absorption bands at 352 nm (π–π*) and 434 nm (n–π*), alongside an enhanced photoisomerization ($\Delta\varepsilon$ = 64.3%) and improved *Z–E* recovery (83.8% conversion). These spectral changes, relative to the neutral condition in DCM (Fig. 2a), may suggest that IHB exists in solution and is effectively disrupted upon treatment with NaOH aq. solution. The resulting increase in switching efficiency further supports the role of IHB in modulating the photochemical behavior of **1a** in solution.

In addition to IHB disruption, the deprotonation of the –COOH group to form $-COO^-$ under basic conditions introduces a distinct change in the electronic structure of **1a**. While the –COOH group acts as an electron-withdrawing group *via* mesomeric effect, deprotonation reduces the net electron-withdrawing character of the substituent, weakening the overall $-M$ effect. Such change alters the conjugation across the azothiophene system, which may contribute to the observed bathchromic shift and influence the stability of the photoisomers. Therefore, both hydrogen bond disruption and electronic

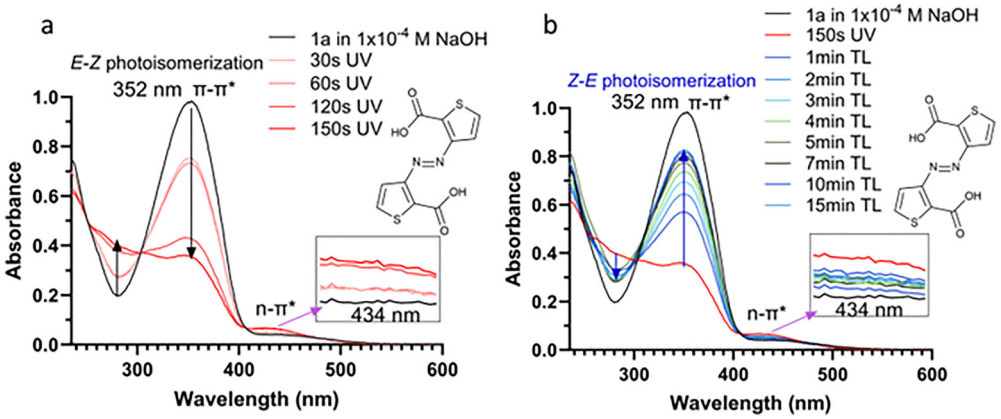

Fig. 4 Time-resolved UV-vis spectra for photoswitching of **1a** using (a) UV light as irradiation source for *E–Z* isomerization, and (b) Tungsten light as irradiation source for *Z–E* isomerization.

mesomeric effects should be considered in understanding the photoswitching behavior of **1a**.

Following this, bidirectional photoisomerization was performed for multiple cycles on molecules **1a** and **1b**, both of which exhibited reversibility and fatigue-resistance through 5 consecutive irradiations with light at 365 nm and 530 nm (Fig. S8). Consequently, all subsequent azothiophenes (with acid groups) were investigated in NaOH aq. solution.

For all other synthesized azothiophenes (**2a–5a**), bearing bulkier or conjugated aromatic systems, the π–π* and n–π* transitions overlapped substantially (Fig. 5), complicating spectral deconvolution.[16]

The spectral shifts in λ_{max} across the azothiophene series reflected trends in conjugation and substitution pattern, Table 1. For instance, molecules **1a** and **1b** exhibit comparably shorter λ_{max} values, both below 377 nm. Substituting one thiophene ring with a salicylic acid moiety (as in **2a**) or a naphthoic acid derivative (**3a**, **4a**, **5a**) extends the π-conjugation and induces bathochromic shifts, increasing λ_{max} to 440 nm and up to 508 nm. This shift is attributed to increased π-conjugation, which reduces the HOMO–LUMO energy gap and shifts λ_{max} into the visible range. Interestingly, a comparison between azothiophenes **3a** and **5a** reveals that hydroxyl substitution at the *para*-position (**3a**) leads to the longest λ_{max} values, whereas *ortho*-substitution (**5a**) results in shorter λ_{max} values. This suggests that, in addition to extended conjugation, the positional orientation of electron-donating groups also plays a key role in tuning the absorption properties of azothiophenes.[45] In terms of photoisomerization efficiency, both **1a** and **1b** azothiophenes exhibited the most significant spectral changes upon irradiation at their respective π–π* wavelengths. In contrast, azothiophenes with increased π-conjugation showed markedly reduced photoresponsiveness, with Δε values below 2.5%, indicating minimal *E*–*Z* isomerization. Notable exceptions include **3a** (14.8%) and **4a** (22.4%), which retained moderate switching behavior (Table 1). These results suggest that increasing aromatic bulk or altering the heterocyclic substitution pattern reduces the extent of *E*–*Z* isomerization, likely due to restricted rotational freedom or increased steric hindrance within the azo framework.[51,52]

The low photoconversion efficiency for compounds **2a–5a** is primarily attributed to significant spectral overlap between the *E* and *Z* isomers, as evidenced by their broad UV-vis spectra (Fig. 5), which complicates selective excitation.[16] This overlap promotes competing photoreactions, limiting the achievable population of the *Z* isomer at the PSS. The potential contribution of a low quantum yield for the *E*–*Z* isomerization or rapid thermal *Z* to *E* relaxation cannot be ruled out

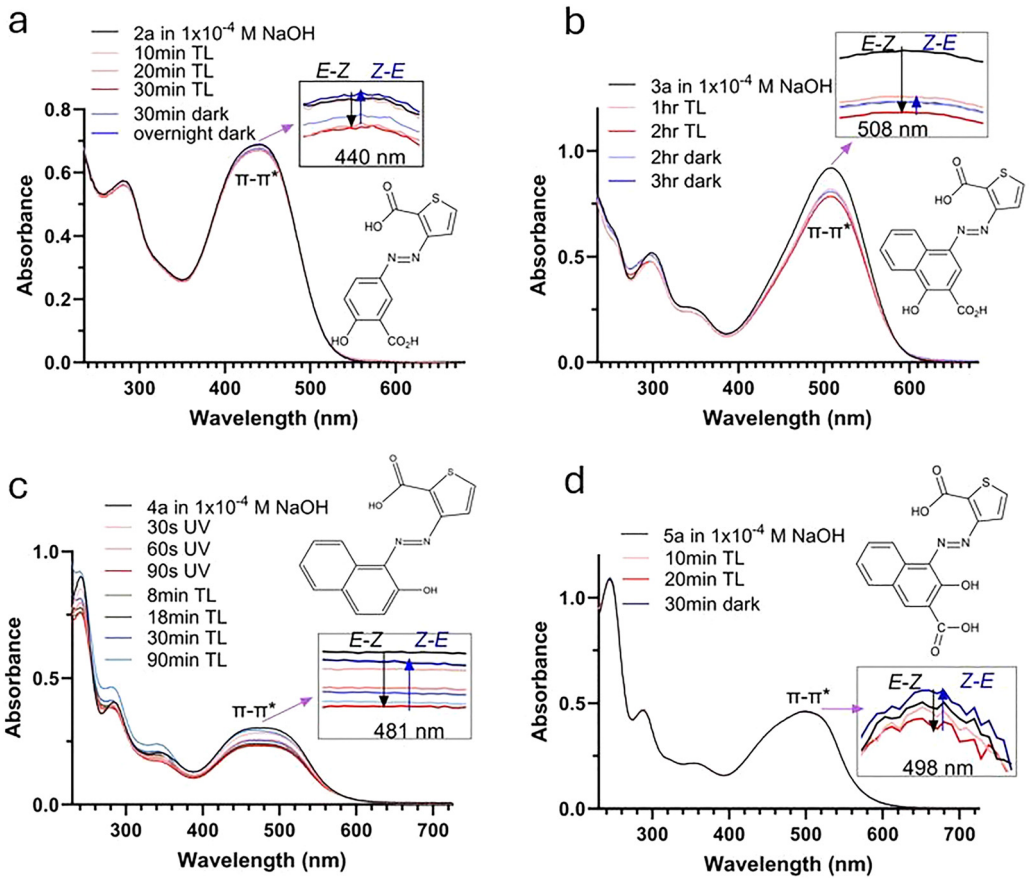

Fig. 5 Time-resolved UV-vis spectra for photoswitching of (a) **2a**, (b) **3a**, (c) **4a**, (d) **5a** in NaOH at room temperature. *Trans*–*cis* photoisomerization was induced by either UV light or Tungsten lamp.

and warrants further investigation through photophysical studies.

To better understand and compare the photoisomerization behavior of neutral molecules **1a** and **1b** in DCM, with experimental $Z \rightarrow E$ conversion yields of 60% and 38%, respectively, activation free energy differences and isomer energy differences were calculated. The absorption wavelengths are shown in Fig. S9, S10 and Tables S6, S7, while the detailed computational results on thermal isomerization are provided in Tables S8–S12 and Fig. S11, S12. The TD-DFT results reproduce the experimental absorption with a difference of 3.4 nm for **1a** molecule and 1.1 nm for **1b** molecule (Table S6), validating the reliability of the computed electronic transitions and their use to interpret band shape and intensity. The weak, red-shifted bands at longer wavelengths can be attributed to low-intensity $n \rightarrow \pi^*$, while the more intense absorptions in the near-UV/blue region arise from strongly allowed $\pi \rightarrow \pi^*$ transitions, consistent with their higher oscillator strengths and experimental extinction coefficients. Importantly, in compound **1b** the intense $\pi \rightarrow \pi^*$ transitions of both isomers lie in the same spectral window, resulting in significant overlap of their absorption envelopes. This overlap provides a rational explanation for the reduced selectivity of excitation and the limited photoconversion at the PSS. By contrast, compound **1a** shows less pronounced overlap between the isomers, consistent with its comparatively higher photochemical switching efficiency (Fig. S9 and S10). Molecule **1a** shows a lower thermal activation free energy in gas phase (80.53 kJ mol^{-1}), and a smaller *E*–*Z* energy difference in DCM (64.67 kJ mol^{-1}) than **1b** (117.27 kJ mol^{-1} and 70.11 kJ mol^{-1}, respectively). This suggests that **1a** is more prone to structural interconversion under thermal conditions, while the larger energy gap in **1b** indicates greater thermodynamic stability of its *E* isomer. Molecules with lower ground-state barriers and smaller thermodynamic asymmetry between isomers often display higher switching yields, as reported for related azo systems.[16,53] This qualitative correlation is consistent with the experimental observation that **1a** undergoes more efficient *Z* to *E* conversion than **1b**. We note that a complete description of the photochemical mechanism would require excited-state potential energy surface (PES) calculations and ultrafast spectroscopic measurements. However, due to limitations in instrumentation and computational resources, we were unable to perform such studies. Nonetheless, our ground-state analysis provides valuable insights into relative stabilities and switching tendencies, consistent with prior reports on azo-based systems.[54]

3.2 Thermal stability

Understanding thermal stability behavior of the *Z* isomer is essential for designing photoswitches with tailored kinetic profiles for a range of applications.[55]

Quantum yields were not measured due to instrumental constraints. Instead, thermal and photo-induced half-lives were obtained, following the methods described in the Experimental section.

Table 2 Thermal stability of the *Z* isomers, half-lives for the thermal *Z*–*E* isomerization measured by ^{1}H NMR in THF-d_8 at 25 °C

Compound	Solvent used	$t_{1/2}$, thermal (days)
1a	THF-d_8	35
1b	THF-d_8	26

The thermal stability of the *Z* isomers, a critical parameter for applications, was quantified by measuring their thermal-induced half-lives ($t_{1/2}$, thermal). As demonstrated in Table 2, molecules **1a** and **1b** exhibit high thermal stability, measuring 35 and 26 days, respectively. The corresponding series of ^{1}H NMR spectra used to monitor the thermal decay and the associated kinetic fitting data are provided in the SI (Fig. S13, S14 and Tables S13, S14).

To evaluate the local environment effects on the photoisomerization process, the photo-induced $Z \rightarrow E$ isomerization of azothiophene **1a** was studied in different solvents with varying polarity. UV-vis absorption spectra were recorded over time following photoirradiation (Fig. S15), and changes in absorbance at the λ_{max} were used to calculate the isomerization kinetics.

Kinetic parameters were extracted by fitting absorbance *vs.* time data to a single-exponential decay function with a time constant parameter (ExpDec1), using Origin 9.1 software (Fig. S16). The exponential time constant (t_1) was used to calculate the rate constant (k) and half-life ($t_{1/2}$, photo) of the $Z \rightarrow E$ transition, based on the following equations,[56]

$$y = y_0 + A_1 \times e^{-\frac{x}{t_1}} \quad (1)$$

$$k = \frac{1}{t_1} \quad (2)$$

$$t_{1/2} = t_1 \times \ln 2 \quad (3)$$

where k (s^{-1}) is the rate constant for a given *Z*–*E* isomerization reaction, and $t_{1/2}$ (s) is the photo-induced *Z* isomer half-life time. TD-DFT calculations revealed a substantial ground-state energy difference of 64.67 kJ mol^{-1} between the *E* and *Z* isomers of **1a**, confirming the significant thermodynamic stability of the *E* isomer. This large energy gap validates the application of a mono-exponential decay model for determining the half-life of the *Z*–*E* relaxation. This approach offers a reliable and reproducible basis for comparing the relative thermal stability under consistent conditions. A more complete kinetic picture, including quantum yields and potential photochemical pathways, will be the focus of future investigations.

The *Z* isomer's photo-induced half-lives, summarized in Table 3, vary significantly across solvents. The fastest isomerization occurred in methanol ($t_{1/2}$, photo-induced = 6 s), and the slowest in THF ($t_{1/2}$, photo-induced = 204 s). A general trend of shorter half-lives with increasing solvent polarity was observed, suggesting enhanced solvation and stabilization of the transition state. Plotting half-lives against solvent polarity (Fig. 6)

Table 3 Photo-induced half-lives ($t_{1/2}$, photo-induced) and other fitting results upon exposure to a tungsten lamp at room temperature for **1a** in several solvents

	t_1 (seconds)	k	$t_{1/2,photo}$ (seconds)	ε
1 M NaOH aq. solution	169.43	0.006	117	80.0
DMSO	25.31	0.04	18	46.45
Acetonitrile	13.83	0.07	10	37.5
Methanol	8.60	0.12	6	32.66
Isopropanol	240.94	0.004	167	18.3
DCM	15.37	0.065	11	8.93
THF	294.65	0.003	204	7.4

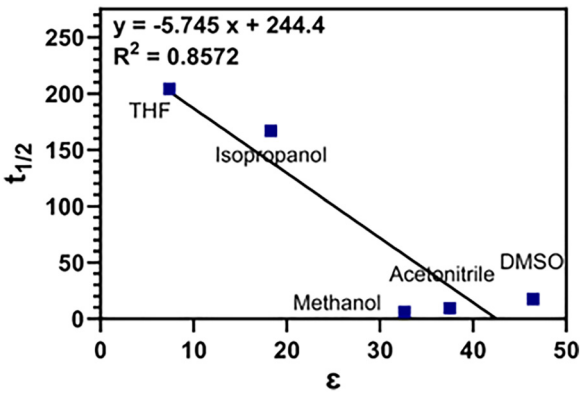

Fig. 6 Calculated half-lives for azothiophene **1a** plotted against solvent polarity.

revealed approximately linear correlation, suggesting that solvent environment influences the stability of isomer.

However, in systems with fast photo- or thermal back-reactions, the observed kinetics may reflect overlapping processes. Particularly in highly polar or protic solvents like methanol, the short half-life may result from rapid back-isomerization at the PSS, affecting the curvature of the decay and leading to interpretation based solely on solvent polarity. Similarly, deviations in half-lives in DCM and NaOH aq. solution likely arise from a combination of electronic effects, hydrogen bonding, and solute-specific interactions. These observations highlight the importance of both molecular properties and kinetic complexities when interpreting thermal stability of a photoswitching molecule, not just bulk solvent polarity.[16]

3.3 Solvatochromic behaviors in different solvents

To assess solvatochromic effects, the π–π* absorption maxima of representative azothiophene derivatives were recorded in a range of solvents varying in polarity and hydrogen-bonding characteristics (Fig. 7). The differences in absorbance intensity between spectra are due to the use of different concentrations to optimize measurement conditions and are not discussed, the detailed concentrations of the employed solvents are presented in Table S15. The solvatochromic behavior results, shown in Table 4, reveal notable shifts in the λ_{max} for several molecules, particularly those bearing electron-donating or withdrawing groups at conjugated positions.

Among them, molecule **3a** exhibited the most pronounced solvatochromic response. Its absorption maximum shifted dramatically from 404 nm in THF to 525 nm in acetone, corresponding to a $\Delta\lambda$ of 121 nm, the largest observed in the series (Table 4). This substantial bathochromic shift indicates a strong sensitivity to solvent environment, likely arising from enhanced intramolecular charge transfer and dipole moment changes in the excited state. In contrast, molecule **4a** showed the smallest solvatochromic response, with only a 17 nm shift across all solvents, suggesting less polarizability or fewer specific solute–solvent interactions. These observations imply that the nature and position of substituents, especially hydroxyl and carboxyl groups, significantly influence solvatochromic behavior.

Interestingly, the changes in λ_{max} do not correlate solely with solvent polarity. For instance, **3a** showed a longer wavelength in acetone (525 nm) than in the more polar methanol (496 nm), indicating other solvent parameters like hydrogen bond acceptor (HBA) and donor (HBD) abilities also contribute to the observed shifts. Molecules **3a**, **4a**, and **5a** contain hydroxyl groups capable of hydrogen bonding with HBA solvents (*e.g.*, DMSO, acetone, DCM, THF), modulating their electronic transitions through interactions with free labile protons, which was later explored.[57]

To further quantify the solvatochromic response of the azothiophenes, the molar electronic transition energy (E_T) was calculated for each molecule in various solvents (Table 4). The E_T values were calculated in kilocalories per mole (kcal mol^{-1}) at room temperature (20 °C) and normal pressure (1 bar), using the Equation.[58,59]

$$E_T\ (\text{kcal mol}^{-1}) = h \times c \times \nu_{max}\ (\text{cm}^{-1}) \times N_A = 28\,591.5/\lambda_{max} \quad (4)$$

where h is Planck's constant, c is the velocity of the light, N_A is Avogadro's number, and ν_{max} and λ_{max} (nm) is the maximum wavenumber and wavelength of the azothiophenes.

The absorption maximum of azothiophenes varies notably across solvents, with significant $\Delta\lambda$ values observed – **3a** showing the largest shift (121 nm) and **4a** the smallest (17 nm). The pronounced solvatochromic response of **3a** suggests its potential as a sensor or probe for detecting changes in solvent polarity. However, the λ_{max} shifts do not completely follow the solvent polarity trends, suggesting that multiple solvent characteristics – such as polarity, basicity, and hydrogen bond acceptor capacity – contribute to the observed behavior. Molecules **3a**, **4a**, **5a** contain hydroxyl groups (*para* in **3a**, *ortho* in **4a**, *ortho* in **5a**) capable of hydrogen bonding with HBA solvents *via* labile protons.[57]

To explain these deviations from polarity-based trends, broader solute–solvent interactions must be considered. Palm *et al.* proposed that both nonspecific (ion/dipole, dipole/dipole, dipole/induced dipole) and specific (H bonding, EPD/EPA interaction) intermolecular forces contribute to solvatochromism.[60] A multiparameter master equation can therefore facilitate the solvent effects on absorption properties.[58]

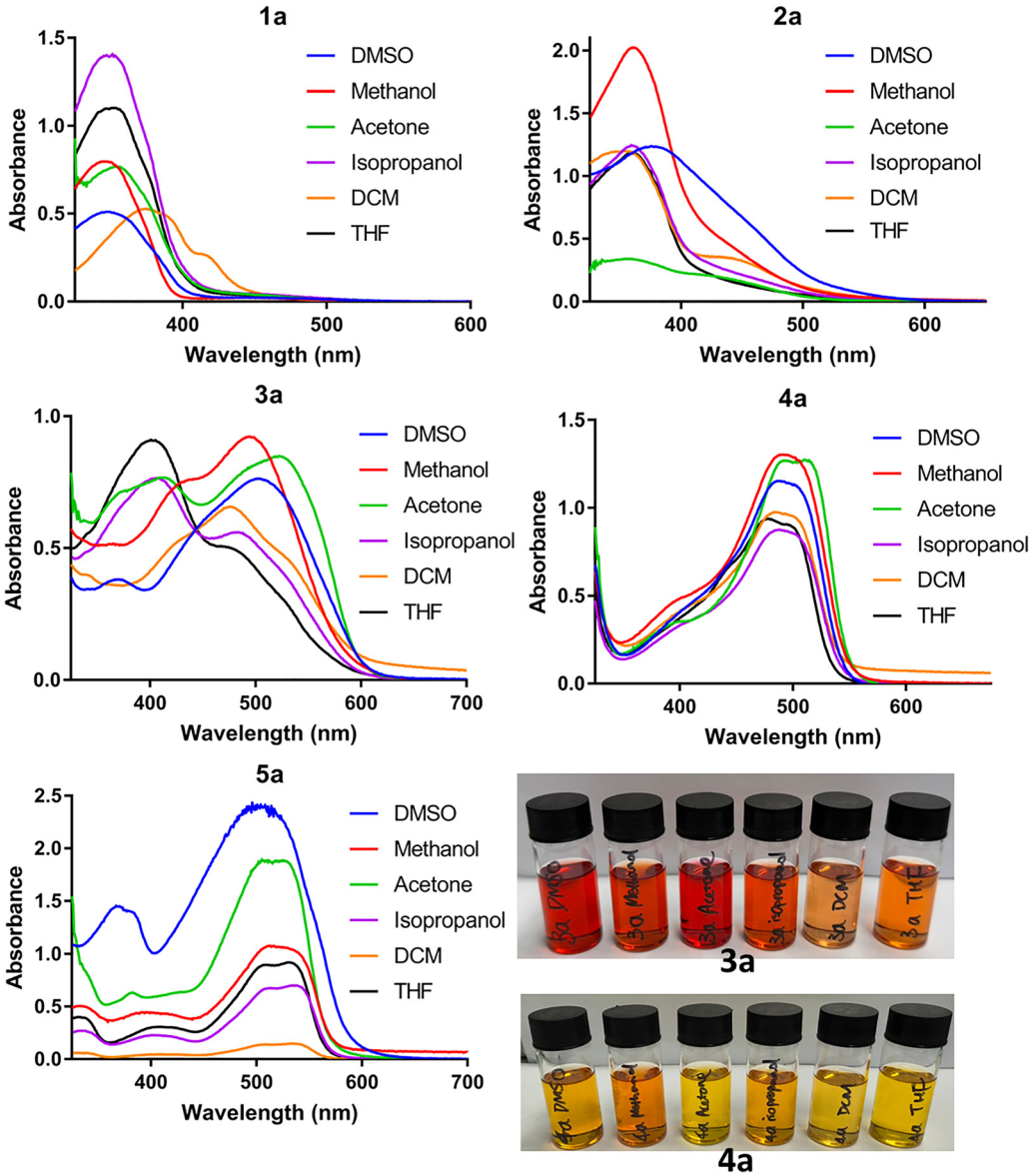

Fig. 7 Solvatochromic UV-vis spectra for five azothiophene molecules. The concentrations were adjusted for each solvent to achieve a suitable absorbance range and were not uniform across solvents, the detailed concentration values are given in Table S15.

Table 4 Absorption maxima (λ_{max}) and molar electronic transition energy (E_T) of azothiophenes (**1a–5a**) in different solvents at 20 °C

		λ_{max} (nm); E_T (kcal mol^{-1})				
Solvents	Dielectric constant at 25 °C	**1a**	**2a**	**3a**	**4a**	**5a**
DMSO	47.2	351; 81.46	377; 75.84	505; 56.62	490; 58.35	505; 56.62
Methanol	32.6	350; 81.69	363; 78.76	496; 57.64	490; 58.35	514; 55.63
Acetone	20.7	356; 80.31	360; 79.42	525; 54.46	495; 57.76	509; 56.17
Isopropanol	20.1	351; 81.46	361; 79.20	487; 58.71	491; 58.23	538; 53.14
DCM	8.9	377; 75.84	349; 81.92	478; 59.81	488; 58.59	537; 53.24
THF	7.4	354; 80.77	360; 79.42	404; 70.77	478; 59.81	532; 53.74

Accordingly, the Kamlet–Abboud–Taft (KAT) linear solvation energy relationship (LSER) model (eqn (5)) was applied, incorporating solvent polarity, hydrogen bond donating, and accepting abilities,[61,62]

$$V = V_0 + s\pi^* + a\alpha + b\beta \quad (5)$$

where V: solute property (wavenumber of maximum absorption), V_0: regression constant, and solvent properties π^*, α, β are

the solvent parameters corresponding to polarity, hydrogen bond donor (HBD) ability, hydrogen bond acceptor (HBA), respectively. The coefficients *s*, *a* and *b* reflect the sensitivity of the solute property to each solvent parameter. Data fitting was performed using the Excel Regression data analysis tool with π*, α and β values provided in Table S16.

The results of the regression fitting are presented in Table S17. Compound **2a** displayed the highest correlation (R^2 = 0.92), followed by **1a** (R^2 = 0.78). Moderate correlation was observed for **5a** (R^2 = 0.55), while **3a** and **4a** showed lower fits (R^2 = 0.48 and 0.32, respectively). These weaker correlations suggest that solvent effects on **3a** and **4a** do not fully captured by the three-parameter KAT model, due to additional factors, such as solvent-assisted azo-hydrazone tautomerization influenced by labile hydroxyl protons (see Section 3.4).

Despite some variability, the KAT analysis offers valuable insights. For azothiophenes **2a** and **3a**, the negative *s*, *a* and *b* coefficients indicate that increasing solvent polarity, HBD acidity, or HBA basicity causes a bathochromic shift, suggesting greater stabilization of the excited state by solvation. In contrast, azothiophenes **1a** and **5a** exhibited positive coefficients, implying hypsochromic shifts and suggesting greater stabilization of the ground state.

The calculated V_{calc} values were plotted against the experimentally observed V_{exp} values in Fig. S17. While linearity correlates with higher R^2 values, the overall trend supports the model's qualitative validity in capturing solvent-dependent spectral behavior.

As shown in Table 5, solvent polarity was the dominant factor influencing absorption for all compounds except **1a**, where HBA basicity played the primary role. This is likely due to the presence of an IHB between the carboxylic acid and azo group in **1a** (as previously confirmed by both X-ray crystallography and UV-vis spectroscopy), which restricts intermolecular hydrogen bonding with the solvent and reduces sensitivity to HBD acidity.

3.4 Azo-hydrazone tautomerism for azothiophene molecules 3a, 4a, 5a

The relatively low LSER model fit for molecules **3a**, **4a**, and **5a** suggests that additional molecular processes – such as azo-hydrazone tautomerism – could influence their solvatochromic behavior. This process, triggered by a labile hydroxyl proton *para* or *ortho* to the azo linkage, leads to proton transfer and structural reorganization between the azo/enol–keto/hydrazone forms, altering both spectral characteristics and photochemical behavior.[63–65] Therefore, the ability of switching between different tautomeric forms makes the azo-hydrazone molecules superior candidates when designing photoswitches with high photoreactivity.[66]

The presence of the hydrazo form was also identified through ^{1}H and ^{13}C analysis of compounds **3a**, **4a** and **5a**, see materials and methods.

As previously shown in Fig. 7, molecule **3a** exhibits two absorption bands in each solvent, attributed to an equilibrium between azo and hydrazone tautomers. The dominant band corresponds to the more stable tautomer under given conditions. The proposed equilibrium between the azo and hydrazone forms is illustrated in Fig. 8.

Studies have shown that the tautomeric equilibration is influenced by substituents (electron-donating, accepting) and the medium environmental conditions such as pH, temperature and polarity.[64,65] To probe this tautomerism, pH-dependent UV-vis experiments were conducted. This method is well-established for identifying azo-hydrazone equilibria, as demonstrated in similar studies.[67,68] While techniques like ^{1}H NMR spectroscopy provide more direct evidence, UV-vis spectroscopy offers reliable and sensitive method for monitoring the equilibrium shift as a function of pH. In DMSO at an apparent neutral pH (7.2, adjusted using an aqueous buffer), two peaks were observed at 505 nm and 456 nm for molecule **3a** (Fig. 9a). Acidification with HCl introduced a new peak at 407 nm (azo form), while the original bands diminished (Fig. 9a). Conversely, under basic conditions (pH 14), the 505 nm band intensified, confirming the dominance of the hydrazone tautomer. These pH-induced spectral shifts – blue shift in acidic and red shift in basic media – consolidate the reversible azo-hydrazone interconversion.

Further experiments in NaOH aq. solution reinforced these findings (Fig. 9b). At pH 12, the 505 nm peak (hydrazone form) was prominent. Lowering the pH below 10 caused a hypsochromic shift to 408 nm (azo form), while raising the pH to 13.2, resulted in the enhancement of the 505 nm band and a slight bathochromic shift in λ_{max} (Fig. 9b). These results confirm the preference for the hydrazone form in basic media, and the azo form in acidic environments. Similarly, the use of acid, base and light as external stimuli was demonstrated by other researchers to investigate the potential of diaryl-hemithioindigos as multi-responsive molecular building blocks.[69]

Table 5 Percentage contributions of three solvatochromic characteristics. Azothiophenes **1a** and **2a** with the high validation of the LSER model fitting

Molecule	Pπ* (%)	Pα (%)	Pβ (%)	R^2
1a	5.5	0.4	94.1	0.78
2a	56.6	0.5	42.9	0.92
3a	67.5	27.9	4.6	0.48
4a	65.5	31.5	3.0	0.32
5a	77.7	10.5	11.8	0.55

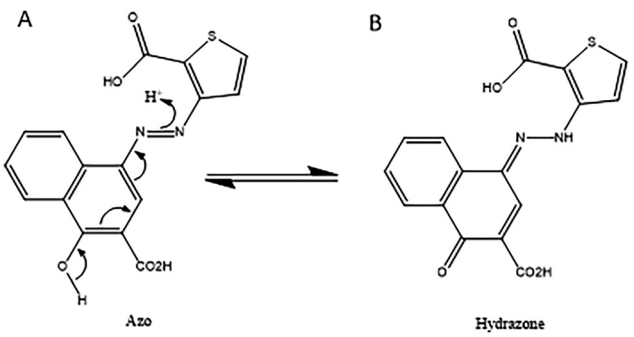

Fig. 8 Proposed azo-hydrazone tautomerism scheme between (A) azo form and (B) hydrazone form, for azothiophene complex **3a**.

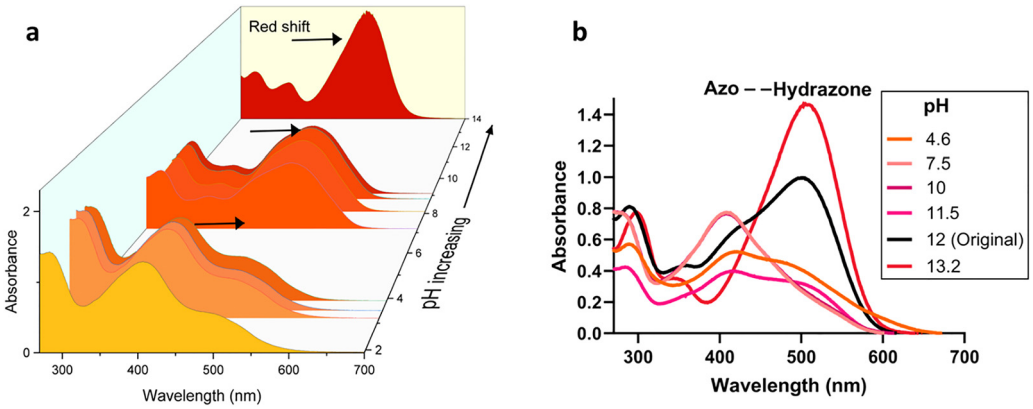

Fig. 9 Azo-hydrazone tautomerism of azothiophene **3a**. (a) 3D waterfall plot for UV-vis spectra for **3a** in DMSO, (b) UV-vis spectra for **3a** in 1×10^{-2} M NaOH aq. solution at varying pH conditions.

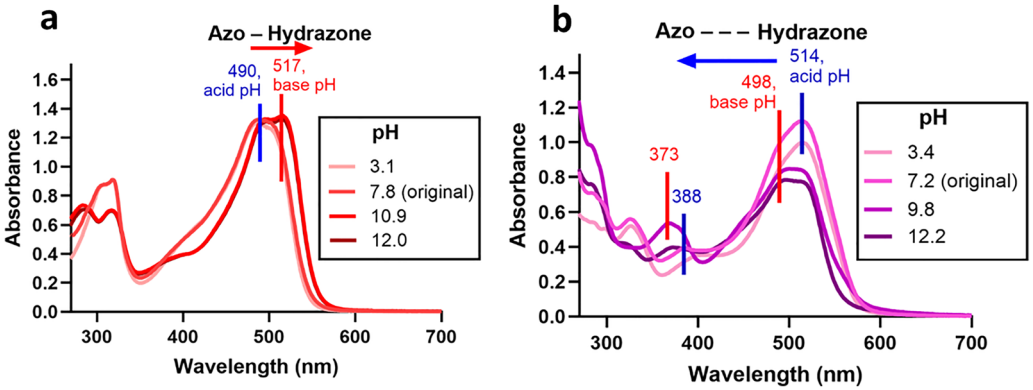

Fig. 10 Azo-hydrazone tautomerism studies on azothiophenes (a) **4a** and (b) **5a**, in the solvent of DMSO, pH of the solution was adjusted using 0.01 M NaOH aq. solution and 0.1 M HCl.

Notably, this tautomerism is accompanied by visible color changes (Fig. S18), attributed to differences in electronic transitions between the aromatic azo and quinoid hydrazone forms. DFT studies support this,[70] showing the hydrazone form has a smaller HOMO–LUMO gap and greater electron delocalization, enhancing n–π* transitions and color intensity. This makes molecule **3a** a promising candidate for pH-responsive sensors or indicators.

Both **4a** and **5a** azothiophenes, which also possess labile hydroxyl protons, were examined similarly (Fig. 10). Molecule **4a** showed minimal spectral response to pH changes, suggesting limited tautomerism. In contrast, **5a** displayed clear tautomeric switching, with distinct peaks at 514 nm and 388 nm corresponding to hydrazone and azo forms, respectively. The pH-sensitive absorption and color changes observed in these synthesized azothiophenes highlight their potential as pH sensors and indicators, which can be used to probe variations in the environment and thus corresponding biochemical process.[32]

4. Conclusions

This contribution reports the successful synthesis and detailed photophysical characterization of five new azothiophene-based dyes with systematically varied structures. Their properties were explored with a focus on $E \leftrightarrow Z$ photoisomerization, solvatochromism, and tautomerism.

All five compounds exhibited differing levels of photoswitching efficiency. Notably, molecules with less bulky aromatic groups (**1a**, **1b**) demonstrated enhanced isomerization, as evidenced by higher *E*–*Z* conversion efficiencies compared to their bulkier analogues (**2a**–**5a**). X-ray crystallographic analysis of **1a** provided insight into molecular conformations, highlighting how specific intramolecular interactions, such as hydrogen bonding can restrict rotational freedom and influence switching behavior. The disruption of intramolecular hydrogen bonding by the addition of a base is not guaranteed at low base equivalents. Consequently, the observed bathochromic shifts and enhanced photoswitching are proposed to be a combined result of (i) weakening/disruption of IHB (when deprotonation is effective) and (ii) changes in electronic distribution after the formation of the carboxylate.

The observed spectral overlap from the experimental data in compounds **2a**–**5a** limits the achievable population of the *Z* isomer, the potential contribution of a low quantum yield for the *E*–*Z* isomerization or rapid thermal *Z* to *E* relaxation can

also contribute to the observed relatively low photoconversion efficiency in compound **2a–5a**, which warrants further investigation.

Thermal relaxation studies showed that **1a** exhibited a longer *Z*-isomer half-life (35 days) than **1b** (26 days). Additionally, photo-induced isomerization from the *Z* to *E* form, along with the formation of a metastable isomer, was investigated to assess its potential applications in photopharmacology.[71] Our findings reveal that the thermal half-lives are not affected solely by bulk solvent polarity but are instead governed by a complex interplay of electronic effects, specific solute–solvent interactions and competing kinetic processes, especially in protic environments.

All acid-functionalized azothiophenes exhibited strong solvatochromic responses, highly dependent on solvent polarity and hydrogen bonding interactions. Linear solvation energy relationships revealed that solvent polarizability had the greatest influence on transition energies, followed by hydrogen bond acceptor ability. Among the series, compound **1a**, with the lowest degree of conjugation, showed the highest sensitivity to HBA effects.

Compound **3a** displayed particularly prominent azo–hydrazone tautomerism, marked by a distinct color change under acidic and basic conditions, highlighting its potential as a pH-responsive dye or sensor. Compounds **3a**, **4a**, and **5a**, bearing carboxylic acid groups, also offer opportunities for further chemical modification, such as bioconjugation or incorporation into hybrid systems.

In summary, this study provides a comprehensive understanding of how substituent structure and solvent environment affect the photophysical behavior of azothiophene dyes. The broad range of observed λ_{max} values and the tunability of photoisomerization properties demonstrate the potential of these molecules as customizable photoswitches for applications requiring precise wavelength responsiveness, environmental sensing, or chemical coupling.

Author contributions

XZ, PH, JW, CCP conceived this research. XZ, KK, DC and JW performed the experiments, NE assisted in tautomerism studies. KK and DC synthesized the compounds. AB conducted the computational investigation. XZ analysed the results. CCP obtained funding for the research and supervised the work. All authors contributed to the writing of the manuscript.

Conflicts of interest

The authors declare no conflict of interest.

Data availability

All data are available from the corresponding author upon request.

The supplementary information (SI) includes the IR and NMR spectra for all synthesized compounds, the complete crystallography data, and details of the data acquisition and processing for the half-life studies, solvatochromic behavior, and computational investigation. Supplementary information is available. See DOI: https://doi.org/10.1039/d5cp03027g.

CCDC 2457289 (**1a**), 2457290 (**1b**) and 2457291 (**1b**) contain the supplementary crystallographic data for this paper.[72a–c]

Acknowledgements

We are sincerely thankful for funding from Air Force Research Laboratory (AFSOR), grants FA9550-20-1-0206 and FA9550-24-1-0274.

References

1 Z. M. Png, C.-G. Wang, J. C. C. Yeo, J. J. C. Lee, N. E. Surat'man, Y. L. Tan, H. Liu, P. Wang, B. H. Tan, J. W. Xu, X. J. Loh and Q. Zhu, *Mol. Syst. Des. Eng.*, 2023, **8**, 1097–1129.
2 M. A. C. Stuart, W. T. S. Huck, J. Genzer, M. Müller, C. Ober, M. Stamm, G. B. Sukhorukov, I. Szleifer, V. V. Tsukruk, M. Urban, F. Winnik, S. Zauscher, I. Luzinov and S. Minko, *Nat. Mater.*, 2010, **9**, 101–113.
3 C. Fedele, T.-P. Ruoko, K. Kuntze, M. Virkki and A. Priimagi, *Photochem. Photobiol. Sci.*, 2022, **21**, 1719–1734.
4 H. Nie, J. L. Self, A. S. Kuenstler, R. C. Hayward and J. de Alaniz, *Adv. Opt. Mater.*, 2019, **7**, 1900224.
5 J. Zhang, Q. Zou and H. Tian, *Adv. Mater.*, 2013, **25**, 378–399.
6 F. Liu and M. W. Urban, *Prog. Polym. Sci.*, 2010, **35**, 3–23.
7 T. Courtney and A. Deiters, *Curr. Opin. Chem. Biol.*, 2018, **46**, 99–107.
8 M. Di Martino, L. Sessa, R. Diana, S. Piotto and S. Concilio, *Molecules*, 2023, **28**(9), 3721.
9 A.-L. Leistner and Z. L. Pianowski, *Eur. J. Org. Chem.*, 2022, e202101271.
10 C. Appiah, K. R. Siefermann, M. Jorewitz, H. Barqawi and W. H. Binder, *RSC Adv.*, 2016, **6**, 6358–6367.
11 S. Jia, W.-K. Fong, B. Graham and B. J. Boyd, *Chem. Mater.*, 2018, **30**, 2873–2887.
12 L. Kortekaas and W. R. Browne, *Chem. Soc. Rev.*, 2019, **48**, 3406–3424.
13 M. Irie, T. Fukaminato, K. Matsuda and S. Kobatake, *Chem. Rev.*, 2014, **114**, 12174–12277.
14 A. Mukherjee, M. D. Seyfried and B. J. Ravoo, *Angew. Chem., Int. Ed.*, 2023, **62**, e202304437.
15 F. A. Jerca, V. V. Jerca and R. Hoogenboom, *Nat. Rev. Chem.*, 2021, **6**, 51–69.
16 H. M. D. Bandara and S. C. Burdette, *Chem. Soc. Rev.*, 2012, **41**, 1809–1825.
17 D. Bléger, J. Schwarz, A. M. Brouwer and S. Hecht, *J. Am. Chem. Soc.*, 2012, **134**, 20597–20600.
18 J. Karcher, S. Kirchner, A.-L. Leistner, C. Hald, P. Geng, T. Bantle, P. Gödtel, J. Pfeifer and Z. L. Pianowski, *RSC Adv.*, 2021, **11**, 8546–8551.

19 J. Lv, Y. Liu, J. Wei, E. Chen, L. Qin and Y. Yu, *Nature*, 2016, **537**, 179–184.
20 G. Xu, S. Li, C. Liu and S. Wu, *Chem. – Asian J.*, 2020, **15**, 547–554.
21 E. Fuentes, M. Gerth, J. A. Berrocal, C. Matera, P. Gorostiza, I. K. Voets, S. Pujals and L. Albertazzi, *J. Am. Chem. Soc.*, 2020, **142**, 10069–10078.
22 S. Municoy, M. I. Álvarez Echazú, P. E. Antezana, J. M. Galdopórpora, C. Olivetti, A. M. Mebert, M. L. Foglia, M. V. Tuttolomondo, G. S. Alvarez, J. G. Hardy and M. F. Desimone, *Int. J. Mol. Sci.*, 2020, **21**, 4724.
23 H. Zhou, C. Xue, P. Weis, Y. Suzuki, S. Huang, K. Koynov, G. K. Auernhammer, R. Berger, H.-J. Butt and S. Wu, *Nat. Chem.*, 2017, **9**, 145–151.
24 P. C. Donthamsetti, J. Broichhagen, V. Vyklicky, C. Stanley, Z. Fu, M. Visel, J. L. Levitz, J. A. Javitch, D. Trauner and E. Y. Isacoff, *J. Am. Chem. Soc.*, 2019, **141**, 11522–11530.
25 W. Szymański, J. M. Beierle, H. A. V. Kistemaker, W. A. Velema and B. L. Feringa, *Chem. Rev.*, 2013, **113**, 6114–6178.
26 J. Volarić, W. Szymanski, N. A. Simeth and B. L. Feringa, *Chem. Soc. Rev.*, 2021, **50**, 12377–12449.
27 J. Otsuki, K. Suwa, K. K. Sarker and C. Sinha, *J. Phys. Chem. A*, 2007, **111**, 1403–1409.
28 S. Crespi, N. A. Simeth and B. König, *Nat. Rev. Chem.*, 2019, **3**, 133–146.
29 D. Gallardo-Rosas, J. M. Guevara-Vela, T. Rocha-Rinza, R. A. Toscano, J. G. López-Cortés and M. C. Ortega-Alfaro, *Org. Biomol. Chem.*, 2024, **22**, 4123–4134.
30 C. E. Weston, R. D. Richardson, P. R. Haycock, A. J. P. White and M. J. Fuchter, *J. Am. Chem. Soc.*, 2014, **136**, 11878–11881.
31 A. S. Matharu, P. B. Karadakov and S. J. Cowling, *Liq. Cryst.*, 2011, **38**(2), 207–232.
32 S. C. Rasmussen, S. J. Evenson and C. B. McCausland, *Chem. Commun.*, 2015, **51**, 4528–4543.
33 C. Slavov, C. Yang, A. H. Heindl, H. A. Wegner, A. Dreuw and J. Wachtveitl, *Angew. Chem., Int. Ed.*, 2020, **59**, 380–387.
34 L. Vautrin, A. Lambert, F. Mahdhaoui, R. El Abed, T. Boubaker and F. Ingrosso, *Molecules*, 2024, **29**, 4053.
35 B. Sentürk, B. Butschke and F. Eisenreich, *Chem. Sci.*, 2025, **16**, 3130–3140.
36 D. M. Adrion and S. A. Lopez, *Org. Biomol. Chem.*, 2023, **21**, 7351–7357.
37 D. M. Adrion and S. A. Lopez, *Org. Biomol. Chem.*, 2022, **20**, 5989–5998.
38 A. H. Heindl and H. A. Wegner, *Chem. – Eur. J.*, 2020, **26**, 13730–13737.
39 R. Diana, L. Sessa, S. Concilio, S. Piotto, L. Di Costanzo, A. Carella and B. Panunzi, *Crystals*, 2024, **14**, 31.
40 C. Averdunk and H. A. Wegner, *Org. Biomol. Chem.*, 2025, **23**, 5805–5811.
41 P. R. Huddleston, V. V. Volkov and C. C. Perry, *Phys. Chem. Chem. Phys.*, 2019, **21**, 1344–1353.
42 M. Glover, P. R. Huddleston and M. L. Wood, *J. Chem. Res.*, 2013, **37**, 43–44.
43 A. Lyčka, *Dyes Pigm.*, 2023, **209**, 110896.
44 Z. Neuerová and A. Lyčka, *Dyes Pigm.*, 2021, **188**, 109149.
45 V. Deneva, A. Lyčka, S. Hristova, A. Crochet, K. M. Fromm and L. Antonov, *Dyes Pigm.*, 2019, **165**, 157–163.
46 A. Lyčka, Z. Vrba and M. Vrba, *Dyes Pigm.*, 2000, **47**, 45–51.
47 P. Gilli, V. Bertolasi, L. Pretto, L. Antonov and G. Gilli, *J. Am. Chem. Soc.*, 2005, **127**, 4943–4953.
48 P. Gilli, V. Bertolasi, L. Pretto, A. Lyčka and G. Gilli, *J. Am. Chem. Soc.*, 2002, **124**, 13554–13567.
49 T. Buffeteau, F. L. Labarthet, M. Pézolet and C. Sourisseau, *Macromolecules*, 2001, **34**, 7514–7521.
50 C. R. Groom, I. J. Bruno, M. P. Lightfoot and S. C. Ward, *Acta Crystallogr., Sect. B: Struct. Sci., Cryst. Eng. Mater.*, 2016, **72**, 171–179.
51 A. B. Grommet, L. M. Lee and R. Klajn, *Acc. Chem. Res.*, 2020, **53**, 2600–2610.
52 A. Gonzalez, E. S. Kengmana, M. V. Fonseca and G. G. D. Han, *Mater. Today Adv.*, 2020, **6**, 100058.
53 M. Irie, *Chem. Rev.*, 2000, **100**, 1685–1716.
54 X. Wang, *Azo Polymers: Soft and Biological Matter*, Springer, 2016, vol. 2.
55 G. Chandra, U. Rani, B. Mahto and G. Kumar Mahato, *Dye Chemistry – Exploring Colour From Nature to Lab*, IntechOpen, 2024.
56 R. Lin, P. K. Hashim, S. Sahu, A. S. Amrutha, N. M. Cheruthu, S. Thazhathethil, K. Takahashi, T. Nakamura, T. Kikukawa and N. Tamaoki, *J. Am. Chem. Soc.*, 2023, **145**, 9072–9080.
57 J. Volarić, W. Szymanski, N. A. Simeth and B. L. Feringa, *Chem. Soc. Rev.*, 2021, **50**, 12377–12449.
58 C. Reichardt, *Chem. Rev.*, 1994, **94**, 2319–2358.
59 C. Reichardt and T. Welton, *Solvents and Solvent Effects in Organic Chemistry*, Wiley, 2010.
60 C.-C. Chiu, C.-C. Hung and P.-Y. Cheng, *J. Phys. Chem. B*, 2016, **120**, 12390–12403.
61 P. W. Carr, *Microchem. J.*, 1993, **48**, 4–28.
62 M. J. Kamlet, J. L. M. Abboud, M. H. Abraham and R. W. Taft, *J. Org. Chem.*, 1983, **48**, 2877–2887.
63 K. Bártová, I. Císařová, A. Lyčka and M. Dračínský, *Dyes Pigm.*, 2020, **178**, 108342.
64 M. A. Rauf, S. Hisaindee and N. Saleh, *RSC Adv.*, 2015, **5**, 18097–18110.
65 S. Kishimoto, S. Kitahara, O. Manabe and H. Hiyama, *J. Org. Chem.*, 1978, **43**, 3882–3886.
66 S. Hristova, F. S. Kamounah, N. Molla, P. E. Hansen, D. Nedeltcheva and L. Antonov, *Dyes Pigm.*, 2017, **144**, 249–261.
67 J. Filo, P. Tisovský, K. Csicsai, J. Donovalová, M. Gáplovský, A. Gáplovský and M. Cigáň, *RSC Adv.*, 2019, **9**, 15910–15916.
68 M. Yahya, R. Metin, B. Aydıner, N. Seferoğlu and Z. Seferoğlu, *Anal. Sci.*, 2023, **39**, 829–842.
69 M. Zitzmann, F. Hampel and H. Dube, *Chem. Sci.*, 2023, **14**, 5734–5742.
70 D. Zheng, Y. Gu, X. Li, L. Zhang, W. Zhao and J. Ma, *J. Chem. Inf. Model.*, 2019, **59**, 2110–2122.
71 M. E. Boëtius, M. W. H. Hoorens, M. Ošťadnický, A. D. Laurent, M. di Donato, A. C. A. van Wingaarden,

M. F. Hilbers, B. L. Feringa, W. J. Buma, M. Medveď and W. Szymanski, *Chem. Sci.*, 2024, **15**, 14379–14389.

72 (*a*) CCDC 2457289: Experimental Crystal Structure Determination, 2025, DOI: 10.5517/ccdc.csd.cc2nh0dl; (*b*) CCDC 2457290: Experimental Crystal Structure Determination, 2025, DOI: 10.5517/ccdc.csd.cc2nh0fm; (*c*) CCDC 2457291: Experimental Crystal Structure Determination, 2025, DOI: 10.5517/ccdc.csd.cc2nh0gn.